Corrosion Science 89 (2014) 220–235

Contents lists available at ScienceDirect

Corrosion Science

journal homepage: www.elsevier.com/locate/corsci

Water vapour effects on corrosion of Fe–Cr and Fe–Cr–Ni alloys containing cerium and manganese in CO_2 gas at 818 °C

Thuan Dinh Nguyen, Jianqiang Zhang, David J. Young *

School of Materials Science and Engineering, University of New South Wales, Sydney, NSW 2052, Australia

ARTICLE INFO

Article history:
Received 16 June 2014
Accepted 21 August 2014
Available online 29 August 2014

Keywords:
A. Rare earth elements
A. Stainless steel
C. Carburisation
C. High temperature corrosion

ABSTRACT

Model alloys Fe–9Cr, Fe–20Cr and Fe–20Cr–20Ni (wt.%) with 0.1% Ce or 2% Mn were exposed to Ar–20CO_2–20H_2O gas at 818 °C, and the results compared with those of reaction with Ar–20CO_2. Water vapour accelerated the corrosion of all Fe–9Cr alloys, and hastened the onset of breakaway oxidation for Fe–20Cr and Fe–20Cr–20Ni. Manganese additions prevented breakaway of the ferritic alloy, and retarded it for the austenitic, but cerium had no effect. All alloys except Mn-bearing variants were simultaneously carburised. Beneficial effects of manganese on high chromium content alloys are discussed in terms of scale phase constitutions.

1. Introduction

Reducing CO_2 emission from coal-fired power plants can be facilitated by the use of oxyfuel combustion, a process in which fuel is burnt in a mixture of oxygen and recirculated flue gas. The resulting flue gas is enriched with both CO_2 and H_2O. Unfortunately, alloy steels used in heat exchangers show accelerated corrosion in CO_2.

The oxidation behaviour of chromium-containing alloys has been studied in dry CO_2 [1–6] and wet CO_2 [5–8] at different temperatures. Adding small amounts of alloying elements like Ce [9] and Mn [4,10] to chromia-forming alloys has been shown to improve their corrosion resistance in a number of environments. However, adding Ce and Mn to Fe–9Cr and Fe–20Cr–20Ni (alloy compositions in weight percent) provided no benefit during exposure to dry CO_2 at 818 °C [4]. In contrast, manganese additions significantly improved the corrosion resistance of Fe–20Cr due to formation of $MnCr_2O_4$ spinel layers in scales, although cerium additions were not beneficial [4].

The aim of this paper was to compare the corrosion of Fe–(9,20)Cr and Fe–20Cr–20Ni containing 0.1% Ce and 2% Mn at 818 °C in wet and dry CO_2, and identify any beneficial effects of the minority alloy additions in the wet gas.

2. Materials and experiments

Nine model alloys, Fe–(9,20)Cr and Fe–20Cr–20Ni with and without 0.1% Ce or 2% Mn, were prepared by arc melting pure metals Fe (99.97%), Cr (99.995%), Ni (99.95%), Mn (99.9%) and Ce (99.9%) under a protective Ar–5%H_2 gas atmosphere, using a non-consumable electrode. The resulting buttons were annealed at 1150 °C for 50 h in flowing Ar–5%H_2 gas for homogenisation. The alloy grain sizes after annealing were 210 ± 180 μm for 9Cr alloys, 2.6 ± 2 mm for 20Cr alloys, and 2.4 ± 1.8 mm for 20Cr20Ni alloys. Rectangular alloy coupons with sizes of (1.3 ± 0.3) mm × (6.5 ± 1) mm × (8.4 ± 1.6) mm were surface ground to a 1200-grit finish and ultrasonically cleaned in alcohol prior to reaction. Analysis by XRD confirmed that Fe–(9,20)Cr–(0.1Ce,2Mn) alloys were ferritic and Fe–20Cr–20Ni–(0.1Ce,2Mn) alloys austenitic.

All specimens were reacted at 818 °C in an Ar–20CO_2–20H_2O (vol.%) mixture with a linear flow rate of 2 cm/s and a total pressure of 1 atm. The water vapour content of the reaction gas was confirmed by a precision dew-point meter (Michell, S8000). Weight changes of oxidised samples were measured using an analytic balance (Precisa 180A) with an accuracy of 0.1 mg. In weight gain kinetic plots shown here, each point represents a separate sample. Corrosion samples were characterised by X-ray diffractometry (XRD; PANanalytical Xpert MPD) with Cu Kα radiation, optical microscopy, scanning electron microscopy (SEM; Hitachi S3400) with an energy dispersive X-ray spectrometer (EDX, Bruker) and transmission electron microscopy (TEM; Philips CM200). Etchants used to reveal carbides and martensite in reacted samples were Murakami's solution (2 g $K_3Fe(CN)_6$ + 2 g KOH + 20 ml H_2O) at 100 °C for Fe–9Cr–(Ce,Mn) alloys, and a modified glyceregia solution (10 ml Glycerine + 6 ml hydrochloric acid + 3 ml HNO_3) at room temperature for Fe–20Cr–(20Ni)–(Ce,Mn) alloys.

* Corresponding author. Tel.: +61 2 9385 4322; fax: +61 2 9385 5956.
E-mail address: d.young@unsw.edu.au (D.J. Young).

http://dx.doi.org/10.1016/j.corsci.2014.08.029
0010-938X/

3. Results

3.1. Corrosion of Fe–9Cr–(Ce,Mn) alloys

Weight gain kinetics for Fe–9Cr–(Ce,Mn) alloys in dry and wet gases are shown in Fig. 1. Observed weight uptakes were large for all alloys, and increased approximately parabolically with time in both gases. Additions of Ce and Mn had no significant effect in either gas, but water vapour increased oxidation rates of all alloys significantly. Scale spallation was not observed for any alloy during cooling. Parabolic rate constants, k_p, were calculated by regression on the equation:

$$\left(\frac{\Delta W}{A}\right)^2 = 2k_p t \quad (1)$$

where $\frac{\Delta W}{A}$ is the weight gain per unit surface area and t the exposure time. Results are summarised in Table 1.

After reaction for 20 h in dry gas [4], Fe–9Cr formed an outer scale layer of FeO, an inner scale layer of ($FeO + FeCr_2O_4$), and an internal oxidation zone (IOZ). Cross-sections of Fe–9Cr–(Ce,Mn) alloys after reaction for 70 h in wet gas are shown in Fig. 2(a–c). The thick scales consisted of multiple oxide layers which were identified by XRD analysis of the surface, removal of surface material by grinding, and repeating the sequence until the underlying alloy was reached. As seen in Fig. 2f, the scale contained an outer layer of Fe_3O_4, an intermediate layer of ($Fe_3O_4 + FeO$), and an inner layer of ($FeO + FeCr_2O_4$). A high magnification image of the intermediate layer on Fe–9Cr in Fig. 2d confirms this layer as being two-phase. Continuous oxide bands in the inner scales linking to intergranular carbides in the underlying alloys were observed for Fe–9Cr–(Ce) (Fig. 2a and b). EDX analysis (not shown) confirmed these oxide bands were (Cr,Fe) rich. A shallow internal oxidation zone (IOZ) developed beneath the scales. Analysis by EDX (not shown) showed that the IOZ in Fe–9Cr–2Mn (Fig. 2e) contained (Cr,Mn)-rich oxide precipitates.

Outer and inner scale thicknesses on Fe–9Cr are shown in Fig. 3 as a function of time in dry and wet gases. Both scale layers grew faster in wet gas than in dry gas.

A high magnification image of the inner scale–alloy interface of Fe–9Cr in Fig. 4a shows that carbides oxidised slower than the alloy during recession of the scale–alloy interface. The remnant intergranular carbide thickness in the inner scale was approximately half that in the adjacent alloy. Analysis by EDX (Fig. 4c) confirmed the presence of intergranular carbides in the inner scale (Fig. 4b).

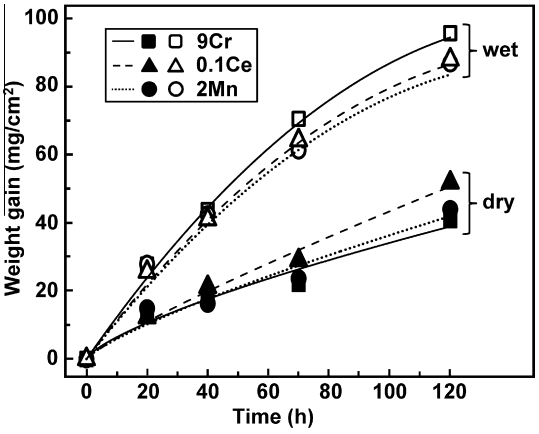

Fig. 1. Weight gain kinetics of Fe–9Cr–(0.1Ce, 2Mn) alloys in Ar–20CO_2 and Ar–20CO_2–20H_2O.

Table 1
Parabolic oxidation rate constant, k_p, for alloys reacted in Ar–20CO_2 and Ar–20CO_2–20H_2O at 818 °C.

Alloy	k_p ($g^2\ cm^{-4}\ s^{-1}$)	
	Ar–20CO_2	Ar–20CO_2–20H_2O
Fe–9Cr	1.8×10^{-9}	1.2×10^{-8}
Fe–9Cr–0.1Ce	3.0×10^{-9}	0.95×10^{-8}
Fe–9Cr–2Mn	2.1×10^{-9}	0.9×10^{-8}
Fe–20Cr	1.2×10^{-12}	9.7×10^{-12}
Fe–20Cr–2Mn	0.39×10^{-12}	0.16×10^{-12}
Fe–20Cr–20Ni	2.4×10^{-10}	1.3×10^{-10}
Fe–20Cr–20Ni–0.1Ce	1.6×10^{-10}	1.5×10^{-10}
Fe–20Cr–20Ni–2Mn	0.08×10^{-10}	0.03×10^{-10}

Cross-sections of inner scales on Fe–9Cr–2Mn after reaction for 20 h in dry and wet gases are shown in Fig. 5. The inner scales contained 2 layers, the outer layer 1 being more dense than the inner layer 2. Coarse porosity was observed in the layer 2. Thicknesses of this layer were about 23 μm in dry gas (Fig. 5a) and 13 μm in wet gas (Fig. 5b). These layers were also observed for Fe–9Cr and Fe–9Cr–0.1Ce. After 120 h reaction, layer 2 still existed and had increased to a thickness of about 32 μm in dry gas (Fig. 6a), but had decreased in wet gas (Fig. 6b). A high magnification image in Fig. 6c shows the presence of grey precipitates and white matrix in the inner scale. Compositional analysis (not shown) showed 18.9 Fe, 21.6 Cr, 4.1 Mn, 55.4 O (all at.%) for the grey precipitates and 46.7 Fe, 2 Cr, 0.8 Mn, 50.5 O for the white matrix, corresponding to (Fe,Cr) spinel precipitates in an FeO matrix.

Porosities of the inner scale layers grown on Fe–9Cr–2Mn were assessed using image analysis of SEM cross-sectional images. Average results for the full width of this layer (Fig. 7) show an increase in porosity with time in dry gas reaction, in contrast with a slight decrease in wet gas reaction.

Internal oxidation depths reached in Fe–9Cr–(Ce,Mn) alloys in dry and wet gases are shown in Fig. 8 as a function of time. The IOZ depths in all alloys in both gases increased initially, and then reached an approximately constant value. As seen from the error bars, the small difference between IOZ thicknesses after oxidation in dry and wet gases is of doubtful significance.

Carburisation products formed in Fe–9Cr–(Ce,Mn) after reaction for 70 h in wet gas are shown in Fig. 9. The Fe–9Cr and Fe–9Cr–0.1Ce alloys (Fig. 9a and b) formed scattered martensite grains and chromium-rich carbides on cooling. Carbide precipitates also formed at the centre (about 0.6 mm deep) of the samples of Fe–9Cr–(Ce). The entire Fe–9Cr–2Mn specimen transformed to martensite after cooling and its fine martensite laths are shown in Fig. 9c. In dry gas, similar carburisation products were observed for each alloy [4]. The volume fraction of intergranular carbides in Fe–9Cr–(Ce) after reaction in dry and wet gases is shown in Table 3. The values were measured in a specific rectangular area (0.23 mm deep × 1.45 mm wide) immediately beneath the IOZ–alloy interface.

3.2. Corrosion of Fe–20Cr–(Ce,Mn) alloys

Weight uptake kinetics for Fe–20Cr–(Ce,Mn) alloys in dry and wet gases are shown in Fig. 10. For Fe–20Cr (Fig. 10a) and Fe–20Cr–0.1Ce (Fig. 10b), weight gains in dry gas were smaller than those in wet gas. Weight uptakes of Fe–20Cr and Fe–20Cr–0.1Ce were approximately equal in wet gas. However, Fe–20Cr–2Mn oxidised slower than the other alloys and had very similar weight gains in both gases (Fig. 10a). No apparent scale spallation was observed for any alloy in either gas. Weight uptake kinetics of Fe–20Cr and Fe–20Cr–2Mn approximately followed the parabolic rate law, and k_p values are summarised in Table 1.